

RESERVE THIS SPACE

Arsenic uptake by pyrite at ambient environmental conditions: a continuous-flow experiment

M. Wolthers¹, I.B. Butler², D. Rickard², P.R.D. Mason¹

¹ Faculty of Geosciences, Utrecht University, Utrecht, The Netherlands

² School of Earth, Ocean and Planetary Sciences, Cardiff University, Cardiff, Wales, U.K

Pyrite was synthesized in the presence of arsenite, As(III), at concentrations approaching those in ambient environments, under controlled, monitored, anoxic conditions in a continuous-flow reaction system at pH 6 and 25°C. During the continuous pyrite growth in these experiments, a continued uptake of arsenic by pyrite was observed. No unequivocal effect of As(III) on the amount of pyrite or on the textures formed was observed. The results presented here demonstrate that a continuous-flow approach to experimentation allows the investigation of contaminant uptake at realistic concentrations. The net result of the reactions studied is the continued fixation of arsenic in pyrite, and the formation of arsenian pyrite. The uptake of arsenic by continuously growing pyrite strongly suggests that arsenic cannot be re-released into solution, unless pyrite is oxidatively dissolved. Furthermore, the synthesis of arsenian pyrite at ambient environmental conditions is in agreement with authigenic arsenian pyrite formed in, for example, marine sediments.

RESERVE THIS SPACE

Introduction

Pyrite is the most stable and ubiquitous authigenic iron(II) sulfide phase in the Earth surface environment. Many different reactions for pyrite, FeS₂, formation at ambient conditions have been suggested (e.g. 1, 2) but detailed mechanistic investigations are exceptional (3–6). A general conclusion is that the formation of the relatively oxidized S₂(–II) disulfide ion is a prerequisite step in any pyrite forming reaction (7). Nucleation of pyrite occurs on existing pyrite surfaces (8, 9), on organic surfaces (10) and, possibly, on defects on the precursor FeS surface (11).

Extensive scavenging of trace elements by pyrite has been previously reported (12, 13). Through this scavenging, pyrite plays an important role in retarding the migration of trace elements in the anoxic environment. Huerta–Diaz and Morse (12) found concentrations of As in marine sedimentary pyrites to be ranging up to 0.93 wt%. Their results indicated that sedimentary pyrite is an important sink for As, even if only minor pyrite formation has taken place.

In a recent study (14, 15), the association of As(V) and As(III) with a nanoparticulate mackinawite, FeS was studied in batch experiments. It was shown that, with increasing initially added As(III) concentrations, the transformation of the pyrite precursor FeS to pyrite is inhibited by stabilization of the precursor FeS surface and (or) prevention of the essential intermediate aqueous FeS cluster complex (cf. 6, 16, 17). However, batch experiments are limited by reactant concentrations and changing conditions during the experiments (14, 15).

Here, the results are reported of a pilot study making use of a chemostatic experimental approach to study dissolved As uptake in iron sulfide systems. Pyrite synthesis in the presence of iron, sulphide and arsenic levels similar to those of natural anoxic sulphidic sediment pore waters, for arsenic that is, 0.02–4.01 μM (18–20) was studied under strictly controlled and monitored conditions in a continuous-flow reaction system (9). Arsenic was added as As(III), which is the dominant aqueous arsenic species in anoxic environments (21–23). The metastable persistence of FeS–H₂S suspensions in the absence of any other electron acceptor is well known (cf. 24, 25, 9). Therefore, pyrite seeds were used to overcome the nucleation barrier and facilitate pyrite formation in order to study As uptake (8). Changes in the solution chemistry were monitored *in situ* via electrodes and *ex situ* by regular sampling and ICP–MS and AAS analyses. The precipitates were characterized by scanning electron microscopy (SEM), X-ray powder diffraction (XRPD) and laser-ablation ICP–MS. The results are interpreted in terms of solution chemistry stability, pyrite textures formed, the effect of arsenic on, and the fate of As(III) during, pyrite formation.

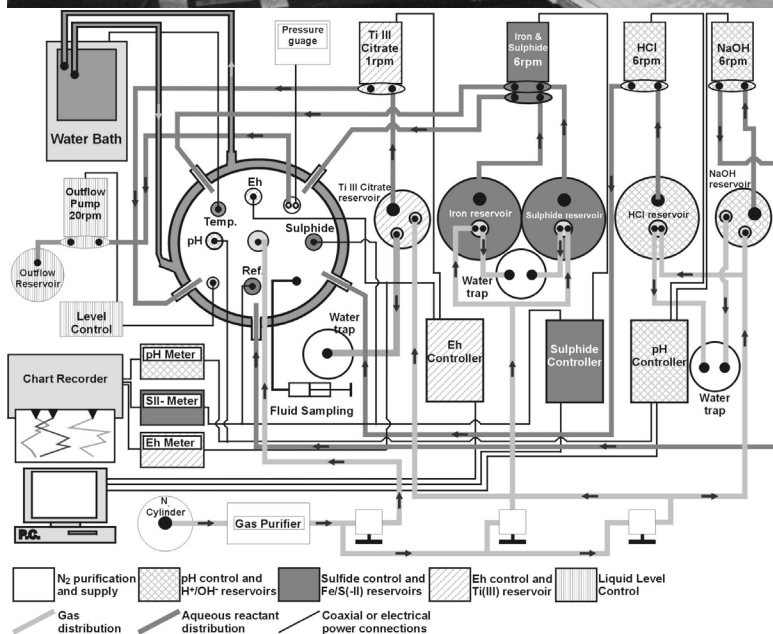
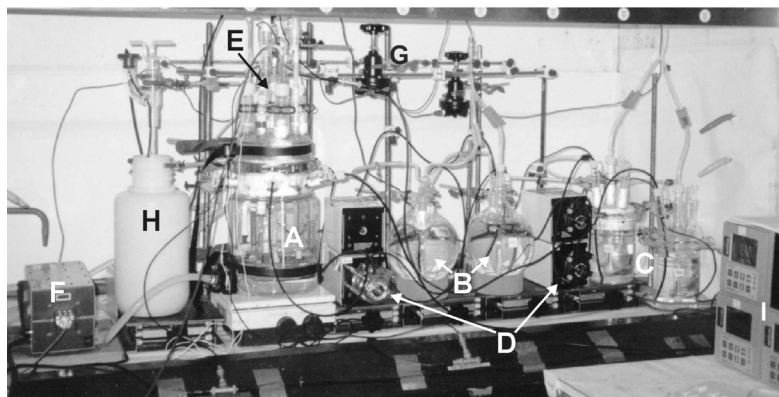


Figure 1. A schematic overview (bottom) and photograph (top) of the continuous flow reaction system (after 9). (A) reaction vessel; (B) iron(II) and sulfide reservoirs; (C) acid and base reservoirs; (D) peristaltic pumps; (E) electrode entries at reaction-vessel head; (F) O₂-free N₂-gas purifier; (G) O₂-free N₂-gas flow-rate control valves; (H) outflow reservoir; (I) process controllers. See text for details.

Materials and methods

Materials

All reagents were analytical grade Fisher Chemicals and used without further purification. Solutions were prepared from 18 M Ω distilled deionized water. The background ionic medium was 0.2 M NaCl. Acid and base solutions were 0.01 M HCl and NaOH, respectively. A 2.0×10^{-3} M sulfide solution was made by dissolving Na₂S·9H₂O. A 6.0×10^{-4} M Fe(II) solution was prepared from Mohr's salt (Fe(NH₄)₂(SO₄)₂·4H₂O). The reaction vessel concentration of Fe(II) was controlled by the FeS solubility, while the S(-II) concentration is not controlled by the FeS solubility due to the excess addition of sulfide. A 1×10^{-2} M As(III) solution was prepared by dissolving NaAsO₂ in deionized water. The Fe(II) solution was spiked with As(III) by adding 0.1 mL of the As(III) solution. The As(III) reservoir concentration was 1.1×10^{-6} M. The solution in the reaction vessel was supersaturated with respect to crystalline orpiment but undersaturated with respect to amorphous As₂S₃ and other crystalline arsenic sulfides during the experimental runs (PHREEQC with the MINTEQ database and solubility data for As₂S₃(am) from 26). Immediately after preparation, the solutions were poured into the O₂-free N₂-filled reservoirs of the chemostat (Figure 1), while vigorously purging with O₂-free N₂, and the reservoirs were sealed. Analytical grade O₂-free N₂ passed through a Supelco high capacity gas purifier to remove traces of O₂ prior to flushing into the reservoirs and the chemostat (Figure 1). Cubic pyrite crystals, purchased at R.G. Widdowson (Scarborough, U.K.), were embedded in Epotech resin. The resin was cut into rectangles with two cm-sized pyrite cubes per block and from each cube one (001) face was exposed by carefully cutting and polishing off the resin. Before inserting the rectangular blocks into the reaction vessel, the quality of the exposed surfaces was investigated by SEM and the pyrite surfaces were cleaned by rinsing with 10% HCl and with acetone and dried. One pyrite face was covered with PTFE tape as a control face.

Continuous-flow reaction system

The custom-built continuous-flow reaction system, or chemostat, in the Cardiff laboratory was used (Figure 1). The main reaction vessel could be sealed air-tight and all connections for electrodes and tubing were air-tight clamped. Purified N₂ was delivered from a Supelco high capacity gas purifier (granular Zr at > 300°C) to the reaction vessel and reservoirs. The temperature in the reaction vessel was controlled at $40 \pm 0.1^\circ$ C. The solution volume was kept constant at 1.00 ± 0.02 L by a vertical float switch and controller connected to a 20 rpm peristaltic pump. The solution was kept

homogenous by magnetic stirring (~60 rpm). The solution conditions in the reaction vessel were monitored using: (i) a gel-filled paper pulp combination pH electrode designed for reliability at high sulfide activity; (ii) a standard combination Pt electrode for redox potential monitoring and; (iii) a Ag/Ag₂S sulfide specific electrode with a double-junction calomel reference electrode (E in Figure 1). The pH electrode was calibrated using Hydrion pH 7.0 and 4.0 buffer solutions. The Pt electrode was checked using Zobell's solution and the sulfide electrode was equilibrated and checked in a concentrated Na₂S·9H₂O solution. The calibrations and electrode checks were performed prior to and after each experimental run. The pH controller was set to keep the pH in the reaction vessel constant at 6.0 ± 0.05 (Table I). The redox potential was not controlled, only monitored. The sulfide controller was set to a constant slow addition of reagents to the reaction vessel at 0.36 mL min^{-1} at 6 rpm via the low-flow (6 rpm) peristaltic pumps. The peristaltic-pump tubing was Masterflex LS13 Viton[®] tubing, which has extremely low O₂ permeability.

Continuous flow method

Before an experiment was started, the reservoirs and reaction vessel were filled and the system was purged with O₂-free N₂ for approximately 24 hours. The reaction vessel was filled with 1 litre of 0.2 M NaCl, to provide an identical electrolyte concentration to that of the reservoir solutions. After sealing the reaction vessel, internal pressure built up and pH and liquid-level control were initiated; after system stabilization, the reactant pumps were started. The As(III)-doped iron(II) solution and the sulfide solution were added via the same peristaltic pump. The initial reaction vessel concentration for all reactants at time zero was zero. As reactants were continually added, the reaction vessel concentrations progressively increased to a stable condition, probably representing a steady state condition, after day 1 in both runs (Table I).

Sampling was done using a syringe and a tube incorporated in the wall of the vessel. Samples of ~40 mL were directly filtered through a Swinnex syringe filter-holder using a 0.2 μm cellulose nitrate membrane filter disk and a Whatman no. 4 glass-fiber prefilter. Subsamples of the filtrate were stored in a sealed glass vial at 4°C until acidification and analysis for total Fe and As. Filter disks were freeze-dried and immediately analyzed by XRPD. At the end of runs, 60 to 80 mL solution was sampled and filtered using a 0.02 μm Millipore filter under a N₂-filled hood. The solid was freeze-dried for ~24 hrs and stored at -18°C until XRPD analysis. Pyrite blocks were removed from the reaction vessel, during and at the end of runs, via a port in the lid. The blocks were washed with deionized water, freeze-dried and immediately Au-coated for SEM analyses. After coating, the blocks were stored in air-tight containers coating silica gel desiccant. After SEM analyses, the blocks were stored at -18°C for LA-ICP-MS analysis.

Analyses

Acidified solution samples were analyzed for total dissolved arsenic using a Perkin Elmer Elan 5000 ICP–MS. The detection limit was 6.5×10^{-9} M (blank $\pm 5 \times \sigma$). Total dissolved iron was measured using a Varian Spectra 300 acetylene-air-flame AAS. The detection limit was 7.4×10^{-9} M (blank $\pm 5 \times \sigma$); errors listed (Table I) are absolute analytical standard deviations. SEM images and energy-dispersive X-ray (EDX) analyses of the Au-coated pyrite blocks were collected on a Leica/Cambridge Instruments S360 SEM. XRPD was carried out using a Philips PW170 based diffractometer (CuK α radiation, 35 kV, 40 mA). Freeze-dried samples on filter disks were loaded into a specimen holder. XRPD patterns, in the range of 3–80° 2 θ , were collected under air using the following settings: 0.1 mm receiving slit, 0.4 s/0.02° 2 θ counting time. Laser-ablation ICP–MS (LA–ICP–MS) analyses of a reacted and an unreacted pyrite block surface were performed using a Micromass Platform ICP equipped with a hexapole device (collision cell) for ion focusing and a quadrupole mass analyzer. Samples were ablated with a Microlas GeoLas 193 nm laser-ablation system, which delivers a homogenized beam at the sample surface, ideal for depth analysis. The system hardware is described in more detail by (27). In order to work at the lowest possible ablation rate of $\sim 0.1 \mu\text{m}$ per pulse, the laser was set to 0.03 GW cm^{-2} irradiance (28). The laser-crater diameter was 120 μm and the pulse repetition rate was 1 Hz.

Results

The experimental conditions during the two runs are listed in Table I. The electrode output signals were relatively stable after one day of reaction. In run 1, the sulfide electrode output was -544 ± 14 mV and in run 2 -534 ± 12 mV. The Eh closely followed the sulfide electrode signal. The total dissolved iron concentration was observed to decrease over the course of the runs, and was continuously below the iron concentration predicted from the iron monosulfide solubility product (29; calculated in MINEQL+ and thermo database). If it can be assumed that sulfide precipitated stoichiometrically with Fe, then the total sulfide concentration in the reaction vessel varied between 8×10^{-4} M (Fe:S = 1:1) and 4×10^{-4} M (Fe:S = 1:2). Dissolved arsenic was $(4.5 \pm 2.9) \times 10^{-9}$ M during the runs, which is $\sim 5\%$ of the reservoir concentration. Thus, the conditions during the runs were stable and comparable between the two runs. The only significant difference was that, to keep the pH static in run 1, approximately twice the amount of acid was needed than in run 2, that is, 0.01 moles H⁺ instead of 0.005 moles.

The suspended-solid concentration was generally too low to yield enough material for XRPD analyses during the runs, except at three days after reaction when the suspended FeS concentration was high enough.

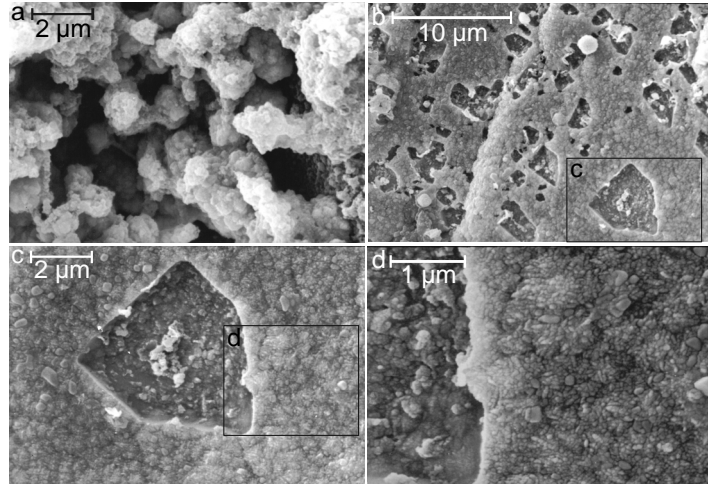


Figure 2. SEM images of (a) FeS precipitate formed on the cubic pyrite surface of pyrite block 1A after 3 days of reaction in run 1; (b) subhedral pyrite formed epitaxially on the pyrite block 1B surface after 9 days of reaction in run 1; (c) and (d) show details of (b).

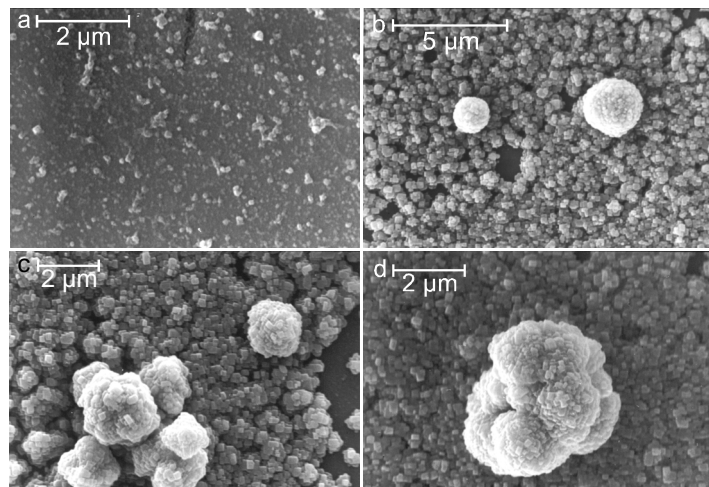


Figure 3. SEM images of products formed on (a) pyrite block 2A after 3 days and (b) – (d) on pyrite block 2B after 9 days of reaction in run 2. (a) the unidentifiable precipitate formed on the still visible cubic pyrite surface; (b) euhedral cubic pyrite overgrowth, formed epitaxially on the cubic pyrite surface, and two solitary proto-framboids (cf. 5) formed on the euhedral-pyrite overgrowth; (c) solitary proto-framboid formed and proto-framboid cluster in the initial stage of forming on the euhedral-pyrite overgrowth; (d) proto-framboid cluster formed on the euhedral-pyrite overgrowth.

Usually, the only diffraction pattern observed was that of NaCl(s) (Table I) from the background ionic medium. A larger volume, sampled from the bottom of the reaction vessel after magnetic stirring was stopped at the end of the runs, yielded enough material to show the presence of pyrite (Table I).

SEM imaging and EDX analyses confirmed the formation of pyrite on the pyrite blocks after 9 days of reaction in runs 1 and 2. In run 1 after 3 days, precipitated FeS was found within holes in the pyrite surface (*pyrite block 1A*, Figure 2a). EDX analysis of the precipitate returned Fe:S ratios characteristic of FeS. The block retrieved after 9 days displayed steps (*pyrite block 1B*, Figures 2b to 2d) and holes in the surface and the precipitate formed as a surface overgrowth consisted of subhedral sub-micrometer sized crystals (Figures 2c and d). Approximately 10% of the surface consisted of holes and cracks in the pyrite block. EDX analysis of the overgrowth (Figure 2b) returned Fe:S ratios characteristic of FeS₂. Analyses of the spherical particles formed on the overgrowth returned Na and Cl signals next to variable Fe:S ratios. Within the overgrowth, regularly shaped holes were observed (Figure 2b). In contrast, after three days in run 2, no SEM-identifiable material was formed (*pyrite block 2A*, Figure 3a). After nine days of reaction in run 2, an overgrowth of submicrometer-sized euhedral pyrite cubes on the surface of the pyrite block was formed and globular pyrite formation occurred on the overgrowth (*pyrite block 2B*, Figures 3b to 3d). Less than 1% of the surface consisted of holes and cracks in the pyrite block. EDX analysis returned ratios characteristic of FeS₂ for both the microcrystalline overgrowth and the globular pyrite.

Figure 4 shows laser-ablation craters formed in the surface of reacted pyrite block 2B, which had been retrieved at the end of run 2. After approximately ten laser pulses, the boundary between the overgrowth and the underlying pyrite block was crossed (b in Figure 4). This corresponds, on the basis of the estimated ablation rate of 100 nm pulse⁻¹, to an overgrowth thickness of ~1 μm, which agrees with an average overgrowth-thickness of ~1 μm estimated from the SEM observations (Figures 3b to 3d). Results from the depth analyses by LA-ICP-MS are plotted in Figure 5. Figure 5a shows the depth profile for the unreacted control surface of pyrite block 2B. At the start of ablation, which is marked by arrow 1 in Figure 5a, the response for ⁵⁷Fe⁺ rapidly increased while the response at masses (i.e., mass/charge or *m/z*) 30, 37 and notably 75 remained unchanged. This shows qualitatively that no arsenic, *m/z* = 75, was present at the surface of unreacted pyrite block 2B. At *m/z* = 30, ³⁰Si⁺ was analyzed simultaneously and the flat response for this isotope shows that no silicate inclusion was ablated. Depth analyses of reacted pyrite block 2B, showed a response-change for ⁵⁷Fe⁺ and ⁷⁵As⁺ at the start of ablation (arrow 1 in Figure 5b). With analysis-time and thus depth, the response for ⁵⁷Fe⁺ remained constant, while the response for ⁷⁵As⁺ dropped to the background level when the boundary between the overgrowth and the underlying pyrite was crossed

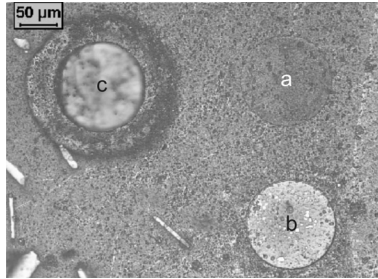


Figure 4. Laser ablation craters in the surface of pyrite block 2B (a) after 5 pulses; (b) after 10 pulses and; (c) after the analysis depicted in Figure 5b. Needle-shaped inclusions in the pyrite (bottom-left corner) are hornblende crystals.

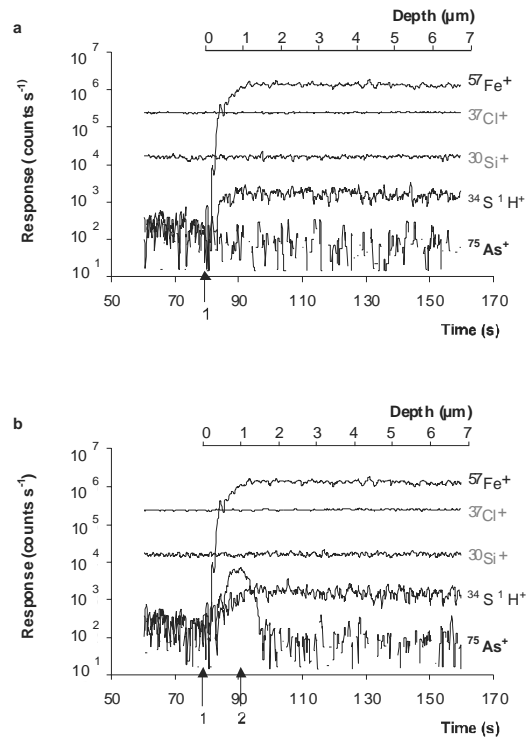


Figure 5. LA-ICP-MS depth profiles of (a) unreacted control section of pyrite block 2B and; (b) reacted section of pyrite block 2B. Arrow 1 marks the start of ablations; arrow 2 marks when the boundary between the overgrowth and the underlying pyrite was crossed. The signals were smoothed by averaging 5 points at equal weight.

(arrow 2 in Figure 5b). Isobaric interferences are possible at $m/z = 75$ from $^{40}\text{Ar}^{35}\text{Cl}^+$ polyatomic ion, which may be produced if the concentration of Cl in the system is high. To test this possibility, $^{37}\text{Cl}^+$ and $^{35}\text{Cl}^+$ were measured simultaneously during the analysis. Since there was no change in the $^{37}\text{Cl}^+$ signal and taking into account that ArCl^+ should form at 100–200 ppm level (27), the $m/z = 75$ cannot be explained by the production of $^{40}\text{Ar}^{35}\text{Cl}^+$. Furthermore, at $m/z = 35$, there was a small but constant increased signal after the start of the ablation which does not correlate with the signal at $m/z = 75$. This signal, which was also observed in the unreacted pyrite block (Figure 5a), is most likely due to the presence of $^{34}\text{S}^1\text{H}^+$ as seen in previous studies (30). The slopes of the curves as a response to concentration changes are not optimal, that is, not near-vertical (28). This is due to the small size of the sample chamber relative to the pyrite block. The resulting large dead volume in the sample chamber causes imperfect mixing of the ablated material and the carrier gas and thus imperfect response times to ablation. However, the depth resolution of the system was sufficient to identify chemical differences between the 1 μm overgrowth and the underlying pyrite.

The results show qualitatively that arsenic was present in the overgrowth formed on the surface of reacted pyrite block 2B. Accurate quantification was not possible as laser ablation is dependent on sample matrix. Suitable matrix-matched metal sulfide standard reference materials which are homogenous at the sub-100 μm scale do not currently exist (e.g. 31). Nevertheless, a semi-quantitative calibration against NIST 612 glass, taking isotopic abundance, ionization efficiency and instrumental response into consideration gave an estimate of 200 ppm As in the FeS_2 . The detection limit for As in pyrite in the EDX analyses was approximately 0.5 wt% (P. Fisher, pers. comm. to I.B.). It can be concluded that the results of the LA-ICPMS and EDX analyses are consistent.

Discussion

Pyrite textures

XRPD analysis showed the formation of pyrite in both runs. However, the pyrite textures formed varied between the two runs. The euhedral overgrowth and globular proto-framboidal pyrite-textures formed in run 2 after 9 days of reaction (Figures 3b to 3d) are identical to the blank runs with single crystal pyrite blocks and no arsenic present (Figure 6a and 6b, see also 9), except for the lack of evidence for framboidal-pyrite formation. However, Butler et al. (9) proposed that the formation of framboidal pyrite

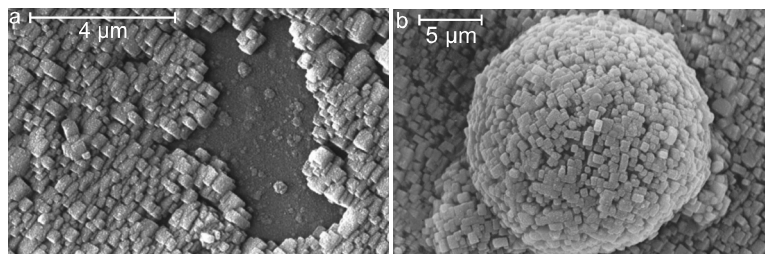


Figure 6. SEM image of the surface precipitates formed on the surface of a pyrite block after 37 days of reaction in a control run, i.e. no arsenic was present; (a) epitaxial pyrite overgrowth; (b) euhedral cubic pyrite overgrowth, formed epitaxially on the cubic pyrite surface, and a solitary framboid. Figures from (9).

in the experiments is partly controlled by hydrodynamics causing diffusion-limited niches in, for example, holes in the pyrite surface. The surface of block 2B was devoid of large holes in the surface, which may explain the lack of framboidal-pyrite formation. In contrast, the pyrite textures formed in run 1 are subhedral (Figures 2b to 2d). Although the subtle controls on pyrite textures developed in experimental systems are not well understood, the pyrite surface and the hydrodynamics are contributing factors controlling the pyrite textures formed (9). The results obtained from the present experiments provide no evidence for a specific control on the pyrite textures. Nevertheless, some important differences between the two runs were observed. After reaction, many more holes were observed at the surface of block 1B, than at the surface of block 2B. Furthermore, steps in the surface of block 1B were observed. Since they were not observed during SEM imaging of the surface prior to reaction, the steps may have formed by dissolution or growth of the pyrite block surface during run 1. Since the surface of block 1B contained more imperfections, the surface may have had more high-energy nucleation sites. This could explain the higher density of crystals formed at the surface of block 1B relative to block 2B. Through spatial constraints, this higher density would limit the size and shape of the crystals formed.

In addition to the relative quality of the surfaces, one significant difference between the two runs was noted: the amount of acid needed to control the pH within the set boundaries. Approximately 0.01 mole of protons was consumed overall in run 1 and ~0.005 mole in run 2. The consumption was faster over the whole period of run 1. Since solution conditions did not vary strongly between the two runs (Table I), this proton consumption must be related to the solid phase. It could, for example, be related to dissolution of inclusions in the pyrite block. The observed steps, holes and regularly shaped “windows” in the pyrite overgrowth (Figure 2b) would support such a dissolution and indicate incomplete removal and coating of inclusions in pyrite block 1B. Other, more subtle differences between the two runs are a slightly lower redox potential as measured by the

Eh electrode, and a stop of several hours in the supply of Fe(II) and sulfide on day 6 of run 1. It may be that the combination of the subtle differences with the differences in surface-quality of the pyrite blocks between runs 1 and 2 has triggered a switch from the formation of pyrite textures identical to previous experiments in the same set-up (9) to the formation of a subhedral texture.

Effect and fate of As(III)

Equilibrium calculations showed that the saturation index for crystalline orpiment, as defined by $SI = \log(I.A.P./K_{sp})$, is > 13 after a steady state has been reached in the reaction vessel for both runs (PHREEQC with MINTEQ database). Using the solubility product for amorphous As_2S_3 from Eary (1992) showed that $As_2S_3(am)$ was continuously undersaturated; also other crystalline As-sulfides were strongly undersaturated. These calculations suggest that arsenic sulfide phases do not control the aqueous As concentration. It is possible that slow As-sulfide formation and continual addition of fresh aqueous arsenite lead to a steady state disequilibrium condition in the reaction vessel where aqueous As concentrations were not controlled directly by orpiment solubility for kinetic reasons. Nevertheless, no heterogeneous As distribution in the epitaxial overgrowth was observed by SEM-EDX, As was continuously below EDX detection limit, nor was a pure arsenic sulfide phase observed by XRD. So the precipitation of a pure As-sulfide mineral seems to be kinetically inhibited at these concentrations and pH, possibly due to the undersaturation with respect to $As_2S_3(am)$ which may otherwise have served as a precursor phase.

The LA-ICP-MS data clearly showed As present in the newly formed pyrite layer. Also, the layer thickness based on ablation rate is consistent with visual observation, and the As concentration in the pyrite layer is semi-quantitatively estimated to be ~200 ppm.

In the highly supersaturated (i.e., nucleation dominated) batch experiments discussed in (14, 15), a strong effect of arsenic on pyrite formation was observed. At arsenic concentrations similar to the arsenic reservoir concentration in the continuous-flow experiments, less pyrite was formed in comparison to arsenic-free control experiments. In the less supersaturated continuous-flow experiments presented here, pyrite crystal growth dominated nucleation during most of the experiment time. During the continuous pyrite growth in these experiments, a continued uptake of arsenic by pyrite is indicated by the constantly low aqueous arsenic concentration. So, previously published experimental results indicate that pyrite nucleation is negatively affected by arsenic (14), the results presented here show that crystal growth is not, or not strongly, affected at similar arsenic concentrations. As discussed above, the pyrite textures varied between the runs, therefore, there is no unequivocal evidence for an effect of As(III) on the textures formed. Nevertheless, the formation of identical textures in run

2 (Figure 3) and in the blanks (Figure 6, see also 9) suggest that As(III) at environmentally realistic concentrations used herein exerts no strong control on the textural development of pyrite.

In view of the data from LA-ICP-MS, thermodynamic modeling and observational results, uptake of As by pyrite is the simplest explanation of the experimental data. The experimental data do not permit the differentiation between adsorption or structural incorporation. Nevertheless, structural incorporation will be preceded by a sorption step and sorption onto a phase which is continuously growing, either by increasing crystal size or the formation of layer upon layer of crystals, will result in the entrapment of arsenic.

Implications

Firstly, the results presented here demonstrate that a continuous-flow approach to experimentation allows the investigation of contaminant uptake at realistic concentrations. Secondly, it is shown that As, at (sub)micromolar concentrations or less, is readily taken up by the neoformed pyrite. Thus, the net result of the reactions in the chemostat is the continued fixation of arsenic in pyrite and, hence, the formation of arsenian pyrite (that is, pyrite containing arsenic). This implies that arsenic cannot be re-released into solution, unless pyrite is oxidatively dissolved. The low solubility of pyrite means that it provides a long term stable sink, limiting As bioavailability in anoxic environments. In addition, the metastable pyrite precursor FeS dissolves to form pyrite (5), and so cannot be regarded as a stable sink for arsenic and other trace elements. Furthermore, the synthesis of arsenian pyrite at ambient environmental conditions is in agreement with authigenic arsenian pyrite formed in, for example, marine sediments (12).

Acknowledgements

Steve Grimes, Anthony Oldroyd and Sarah Goldsmith (Cardiff University), Cornelis Woensdregt, Cornelis van der Weijden (Utrecht University) and Peter van der Linde (University of Professional Education Leiden) are acknowledged. The manuscript was improved by the valuable comments of three anonymous reviewers and the associate editor. This research was supported by NWO/ALW grant 750.197.06 to M.W. and NERC grant NERLS200000611 to D.R. The Utrecht LA-ICP-MS lab was supported by the NWO/GOA. This research was conducted under the program of the Netherlands Research School of Sedimentary Geology.

References

1. Morse, J.W.; Millero, F.J.; Cornwell, J.C.; Rickard, D., The Chemistry of the Hydrogen Sulfide and Iron Sulfide Systems in Natural Waters. *Earth–Sci. Rev.* **1987**, *24*, 1–42.
2. Wilkin, R.T.; Barnes, H.L., Formation processes of framboidal pyrite. *Geochim. Cosmochim. Acta* **1997**, *61*, 323–339.
3. Rickard, D., Kinetics and mechanism of pyrite formation at low temperatures. *Am. J. Sci.* **1975**, *275*, 636–652.
4. Luther, III G.W., Pyrite synthesis via polysulfide compounds. *Geochim. Cosmochim. Acta* **1991**, *55*, 2839–2849.
5. Rickard, D., Kinetics of pyrite formation by the H₂S oxidation of iron(II) monosulfide in aqueous solutions between 25 and 125°C: The rate equation. *Geochim. Cosmochim. Acta* **1997**, *61*, 115–134.
6. Rickard, D.; Luther, III G.W., Kinetics of pyrite formation by the H₂S oxidation of iron (II) monosulfide in aqueous solutions between 25 and 125°C: The mechanism. *Geochim. Cosmochim. Acta* **1997**, *61*, 135–147.
7. Tossell, J.A.; Vaughan, D.J.; Burdett, J.K., Pyrite, marcasite and arsenopyrite type minerals: crystal chemical and structural principles. *Phys. Chem. Min.* **1981**, *7*, 177–184.
8. Harmandas, N.G.; Fernandez, E.N.; Koutsoukos, P.G., Crystal growth of pyrite in aqueous solutions. Inhibition by organophosphorus compounds. *Langmuir* **1998**, *14*, 1250–1255.
9. Butler, I.B.; Rickard, D.; Grimes, S.T.; Oldroyd, A., Nucleation and growth of pyrite on pyrite seeds. *Abstr. Pap. Am. Chem. Soc.* **2003**, *225*.
10. Grimes, S.T.; Brock, F.; Rickard, D.; Davies, K.L.; Edwards, D.; Briggs, D.E.G.; Parkes, R.J., Understanding fossilization: experimental pyritization of plants. *Geology* **2001**, *29*, 123–126.
11. Wang, Q.; Morse, J.W., Pyrite formation under conditions approximating those in anoxic sediments I. Pathway and morphology. *Mar. Chem.*, **1996**, *52*, 99–121.
12. Huerta-Diaz, M.A.; Morse, J.W., Pyritization of trace metals in anoxic marine sediments. *Geochim. Cosmochim. Acta* **1992**, *56*, 2681–2702.
13. Morse, J.W.; Luther, III G.W., Chemical influences on trace metal-sulfide interactions in anoxic sediments. *Geochim. Cosmochim. Acta* **1999**, *63*, 3373–3378.
14. Wolthers, M., Geochemistry and environmental mineralogy of the iron-sulphur-arsenic system. PhD thesis. Geologica Ultraiectina 225. 2003.
15. Wolthers, M.; Butler, I.B.; Benning, L.; Rickard, D.; in prep. Arsenic in iron sulphides: sorption and incorporation.
16. Butler, I.B.; Grimes, S.T.; Rickard, D., Pyrite formation in an anoxic chemostated reaction system. *J. Conf. Abs.* **2000**, *5*, 274–275.
17. Rickard, D.; Butler, I.B.; Oldroyd, A., A novel iron sulphide mineral switch and its implications for Earth and planetary science. *Earth Planet. Sci. Lett.* **2001**, *189*, 85–91.

18. Widerlund, A.; Ingri, J., Early diagenesis of arsenic in sediments of the Kalix River estuary, northern Sweden. *Chem. Geol.* **1995**, *125*, 185–196.
19. Yan, X-P.; Kerrich, R.; Hendry, M.J., Distribution of arsenic(III), arsenic(V) and total inorganic arsenic in porewaters from a thick till and clay-rich aquitart sequence, Saskatchewan, Canada. *Geochim. Cosmochim. Acta* **2000**, *64*, 2637–2648.
20. Sullivan, K.A.; Aller, R.C., Diagenetic cycling of arsenic in Amazon shelf sediments. *Geochim. Cosmochim. Acta* **1996**, *60*, 1465–1477.
21. Andreae, M.O., Arsenic speciation in seawater and interstitial waters: The influence of biological-chemical interactions on the chemistry of a trace element. *Limnol. Oceanogr.* **1979**, *24*, 440–452.
22. Sadiq, M., Arsenic chemistry in marine environments: a comparison between theoretical and field observations. *Mar. Chem.* **1990**, *31*, 2850–297.
23. Kuhn, A.; Sigg, L., Arsenic cycling in eutrophic Lake Greifen, Switzerland: influence of seasonal redox processes. *Limnol. Oceanogr.* **1993**, *38*, 1052–1059.
24. Schoonen, M.A.A.; Barnes, H.L., Reactions forming pyrite and marcasite from solution: I. Nucleation of FeS₂ below 100°C. *Geochim. Cosmochim. Acta* **1991**, *55*, 1495–1504.
25. Benning, L.; Wilkin, R.T.; Barnes, H.L., Reaction pathways in the Fe-S system below 100°C. *Chem. Geol.* **2000**, *167*, 25–51.
26. Eary, L.E., The solubility of amorphous As₂S₃ from 25 to 90°C. *Geochim. Cosmochim. Acta* **1992**, *56*, 2267–2280.
27. Mason, P.R.D.; Kraan, J.W., Attenuation of spectral interferences during laser ablation inductively coupled plasma mass spectrometry (LA-ICP-MS) using an rf only collision and reaction cell. *J. Anal. At. Spectrom.* **2002**, *17*, 858–867.
28. Mason, P.R.D.; Mank, A.J.G., Depth-resolved analysis in multi-layered glass and metal materials using laser ablation inductively coupled plasma mass spectrometry (LA-ICP-MS). *J. Anal. At. Spectrom.* **2001**, *16*, 1381–1388.
29. Davison, W.; Philips, N.; Tabner, B.J., Soluble iron sulfide species in natural waters: reappraisal of their stoichiometry and stability constants. *Aquat. Sci.* **1999**, *61*, 23–43.
30. Mason, P.R.D.; Kaspers, K.; Van Bergen, M.J., Determination of sulfur isotope ratios and concentrations in water samples using ICP-MS incorporating hexapole ion optics. *J. Anal. At. Spectrom.* **1999**, *14*, 1067–1074.
31. Nesbitt, R.W.; Hirata, T.; Butler, I.B.; Milton, J.A., UV Laser Ablation ICPMS: Some Applications in the Earth Sciences. *Geostandards Newsletter* **1998**, *20*, 231–243.

Table I. Data for runs 1 and 2. p_{rv} = pressure, in mbar above ambient pressure, in the reaction vessel; S(-II) and Eh are the uncalibrated raw millivolt signals from, respectively, the sulfide and redox potential electrodes; $[Fe]_{aq}$ is the total dissolved iron concentration measured by AAS; $[As]_{aq}$ is the arsenic concentration measured by ICP-MS; in the XRPD column the XRPD-identifiable products are listed, Py = pyrite. See text for detection limits and standard deviations.

<i>Run</i>	<i>Day</i>	p_{rv} (mbar)	<i>pH</i>	<i>S(-II)</i> (mV)	<i>Eh</i> (mV)	$[Fe]_{aq}$ ($\times 10^{-5} M$)	$[As]_{aq}$ ($\times 10^{-8} M$)	<i>XRPD</i>	<i>Remarks</i>
1	0	21	6.05	-123	-222				Start of reagent pumps
	1	22	6.07	-530	-347				
	2	25	5.98	-535	-354	3.76 ± 0.07	2.7 ± 1.3	NaCl + FeS	
	3	23	6.03	-539	-359	3.12 ± 0.04	5.3 ± 1.3	NaCl	Pyrite block 1A retrieved
	4	20	6.07	-548	-356				
	5	22	6.01	-547	-356				
	6	35	6.08	-558	-363	2.04 ± 0.04	2.7 ± 1.3	NaCl	
	7	27	6.02	-550	-360	2.90 ± 0.04	5.3 ± 1.3	NaCl	
	8	27	6.09	-548	-354	2.72 ± 0.06	6.7 ± 1.3	NaCl	
9	29	6.12	-551	-350	2.15 ± 0.03	5.3 ± 1.3	NaCl + Py	Pyrite block 1B retrieved	
2	0	27	6.05	-70	-137				Start of reagent pumps
	1	35	6.02	-522	-321				
	2	28	5.98	-532	-333	4.72 ± 0.06	6.7 ± 1.3	NaCl + FeS	
	3	22	6.09	-528	-334	4.83 ± 0.02	9.3 ± 1.3	NaCl	Pyrite block 2A retrieved
	4	33	6.05	-527	-328				
	5	36	6.04	-532	-335				
	6	38	6.05	-538	-342				
	7	38	6.03	-547	-353	2.08 ± 0.01	d.l.	NaCl	
	8	37	6.05	-546	-393	2.44 ± 0.01	1.3 ± 1.3	NaCl	
9	39	6.10	-545	-392			NaCl + Py	Pyrite block 2B retrieved	